Space Weather

RESEARCH ARTICLE
10.1029/2024SW003950

On the Performance of a Real-Time Electron Radiation Belt Specification Model

Frances Staples[1], **Adam Kellerman**[1], **and Janet Green**[2]

[1]Department of Atmospheric & Oceanic Sciences, University of California, Los Angeles, CA, USA, [2]Space Hazards Applications, LLC, Arapahoe St Golden, CO, USA

Key Points:

- Real-time data-assimilative hindcasts of the outer electron radiation belt were accurate to within a factor of 1.5
- Data assimilation substantially improved the error and bias of radiation belt specification but strongly influenced hindcast error and bias
- Improved physics-based modeling and continuous real-time observations through the outer radiation belt are needed for accurate hindcasts

Supporting Information:

Supporting Information may be found in the online version of this article.

Correspondence to:

F. Staples,
fastaples@atmos.ucla.edu

Citation:

Staples, F., Kellerman, A., & Green, J. (2024). On the performance of a real-time electron radiation belt specification model. *Space Weather*, *22*, e2024SW003950. https://doi.org/10.1029/2024SW003950

Received 3 APR 2024
Accepted 22 NOV 2024

Author Contributions:

Conceptualization: Adam Kellerman, Janet Green
Data curation: Adam Kellerman
Formal analysis: Frances Staples
Methodology: Frances Staples, Adam Kellerman
Supervision: Adam Kellerman
Validation: Frances Staples
Writing – original draft: Frances Staples
Writing – review & editing: Frances Staples, Adam Kellerman, Janet Green

Abstract Maintaining accurate real-time hindcast and forecast specification of the radiation environment is essential for operators to monitor and mitigate the effects of hazardous radiation on satellite components. The Radiation Belt Forecasting Model and Framework (RBFMF) provides real-time forecasts and hindcasts of the electron radiation belt environment, which are used as inputs for the Satellite Charging Assessment Tool. We evaluated the long-term statistical error and bias of the RBFMF by comparing the 10-hr hindcast of electron phase space densities (PSD) to a multi-mission data set of PSD observations. We found that, between the years 2016–2018, the RBFMF reproduced the radiation belt environment to within a factor of 1.5. While the error and bias of assimilated observations were found to influence the error and bias of the hindcast, data assimilation resulted in more accurate specification of the radiation belt state than real-time Van Allen Probe observations alone. Furthermore, when real-time Van Allen Probe observations were no longer available, the hindcast errors increased by an order of magnitude. This highlights two needs; (a) the development of physics-based modeling incorporated into this framework, and (b) the need for real-time observations which span the entire outer radiation belt.

Plain Language Summary It is important to accurately predict and monitor the radiation levels in space to safeguard satellites from potential damage. This paper introduces a model called the Radiation Belt Forecasting Model and Framework, which provides real-time forecasts and historical data (hindcasts) of radiation levels. To test the model's accuracy, we compared its predictions to actual observations from satellites between 2016 and 2018. We found that generally, the model's predictions of the outer radiation belt were within 1.5 times of the actual measurements. Additionally, we discovered that incorporating both real-time satellite observations and physics-based simulation improved prediction accuracy compared to relying solely on either method. However, we noticed a significant increase in prediction errors when real-time observations through the heart of the Van Allen radiation belt were unavailable. This underscores the importance of enhancing the model with physics-based modeling and ensuring continuous real-time observations of radiation levels in space.

1. Introduction

The variability of the near-Earth radiation environment poses a serious hazard to telecommunications, navigational, and defense satellites which orbit through these regions. A key effect of spacecraft exposure to radiation is internal charging, where high energy electrons penetrate the surface shielding of a satellite and deposit charge into dielectric materials such as circuit boards or cable insulators, and on ungrounded material such as spot shields or connector contacts (e.g., Fennell et al., 2001; Lohmeyer et al., 2015). The accumulated charging eventually results in electrostatic discharges, which is one of the known causes of "satellite anomalies." Anomalies range in effect from more frequent temporary errors in non-critical systems to rare but catastrophic hardware damage and complete mission failure (Galvan et al., 2014) and can be instigated by a number of issues, such as command errors, manufacture flaws, and environmental exposures. Of all space environment effects on satellites, electrostatic discharges from internal charging have been reported to cause the most anomalies (Green et al., 2017; Koons et al., 1999).

Improved on-orbit anomaly detection tools have been cited by satellite operators as an industrial need for operators to easily and quickly attribute anomalies to space weather effects (Green et al., 2017). To attribute satellite anomalies to internal charging of equipment requires forensic reconstruction of the radiation environment and modeling of charge accumulation on component hardware, such as satellite shielding materials, for defined orbits (LEO, MEO, GEO). The Satellite Charging Assessment Tool (SatCAT: Green et al., 2017, 2020) is one such tool which allows users to monitor the real-time and long-term effects of internal charging due to fluence of radiation belt electrons. This paper evaluates the Radiation Belt Forecasting Model and Framework (RBFMF) which SatCAT uses to specify the radiation environment both retrospectively and in real-time.

Several models have been developed to simulate the near-Earth radiation environment based upon the Van Allen radiation belt response to solar wind parameters and/or geomagnetic indices. These models usually fall within three categories; empirically based analytical descriptions (e.g., X. Li, 2004; Nagai, 1988; Roeder et al., 2005; Turner & Li, 2011), physics-based models (e.g., Horne et al., 2013; Subbotin & Shprits, 2009), and machine learning models (e.g., Boyd et al., 2023; Chen et al., 2019; Wei et al., 2018). Statistical approaches to modeling the radiation belt have shown success at identifying the key variables which influence radiation belt flux on different timescales. However, statistical approaches do not capture some extreme events, and could be flawed if they cannot reflect the non-linear relationship between input variables are output electron fluxes. While physics-based modeling allows the study of relative contributions of complex acceleration and loss mechanisms in the outer radiation belt, the computational power required to accurately model the interconnected magnetospheric system on an hourly basis provides a significant challenge. Machine learning models have predicted ultra-relativistic electron fluxes with high efficacy but show less accuracy at predicting lower energy fluxes (Camporeale, 2019; Shin et al., 2016), similarly to statistical modeling, could have limited capabilities for extreme events which are out of sample to training data.

Hindcast models that rely on existing data, such as RB-Daily-E (Gabrielse et al., 2022), have performed well at capturing past events and relating them to spacecraft anomalies. For example, RB-Daily-E ingested Van Allen Probe data to build a hindcast of the radiation belts, demonstrating solar cell voltage degradation was due to the radiation environment whereas the current degradation was largely due to other factors. However, these models are unable to forecast the radiation belt environment. By dynamically integrating observational data with lightweight statistical or physics-based model predictions of the radiation belt, data assimilative frameworks could improve the accuracy and responsiveness to real-time changes, thereby providing more reliable and timely forecasts then statistic or physics-based modeling methodologies used alone.

Several such frameworks have recently been designed to address specific forecasting or hindcasting goals. For example, SPACESTORM (Glauert et al., 2018) captures the long term climatology of the radiation belt by assimilating GOES electron observations to determine the outer boundary condition of the BAS-RBM diffusion model (Glauert et al., 2014). The PAGER framework (du Montcel et al., 2023) integrated VERB-3D diffusive modeling of the radiation belt (Subbotin & Shprits, 2009) with GOES-16 observations to calculate internal charging risk due to electrons on a daily basis. The SafeSpace model (Brunet et al., 2023) was developed to provide daily activity indices of radiation belt risk from electrons and protons using complex prototype of Sun-to-Earth modeling pipeline driving diffusive radiation belt simulations using the Salammbô - EnKF code (Bourdarie & Maget, 2012).

RBFMF was developed to provide a lightweight and robust tool for real-time radiation belt specification which operates on an hourly basis. This framework uses 1D Kalman filtering technique which has previously been shown through event-based studies to be a successful tool for reproducing the radiation belts (e.g., Coleman et al., 2018; Daae et al., 2011; Kellerman et al., 2014). This work investigates the hindcast performance of RBFMF by completing a detailed statistical evaluation of archived multi-year data set. Special focus is given to the hindcast rather than the forecast because the hindcast includes assimilated data and is therefore a more accurate representation of the environment and useful for post-anomaly attribution by satellite operators. We aim to assess how data assimilation affects the error and bias of radiation belt hindcasts, and the influence of variable geomagnetic conditions. In this way, we identify how the RBFMF may be adapted in the future for improved hindcast reliability.

2. Radiation Belt Forecasting Model and Framework

The radiation belt forecast framework (RBFMF) is designed to combine physics-based modeling with data assimilative techniques to provide forecasts, nowcasts, and hindcasts of the radiation environment in real-time on an hourly basis. In this framework, real-time space weather data from GOES and the Van Allen Probes is assimilated into a diffusive simulation of the radiation belt (Subbotin & Shprits, 2009) using an existing data assimilative model (Shprits et al., 2013). The framework has been further developed (Kellerman, 2018;

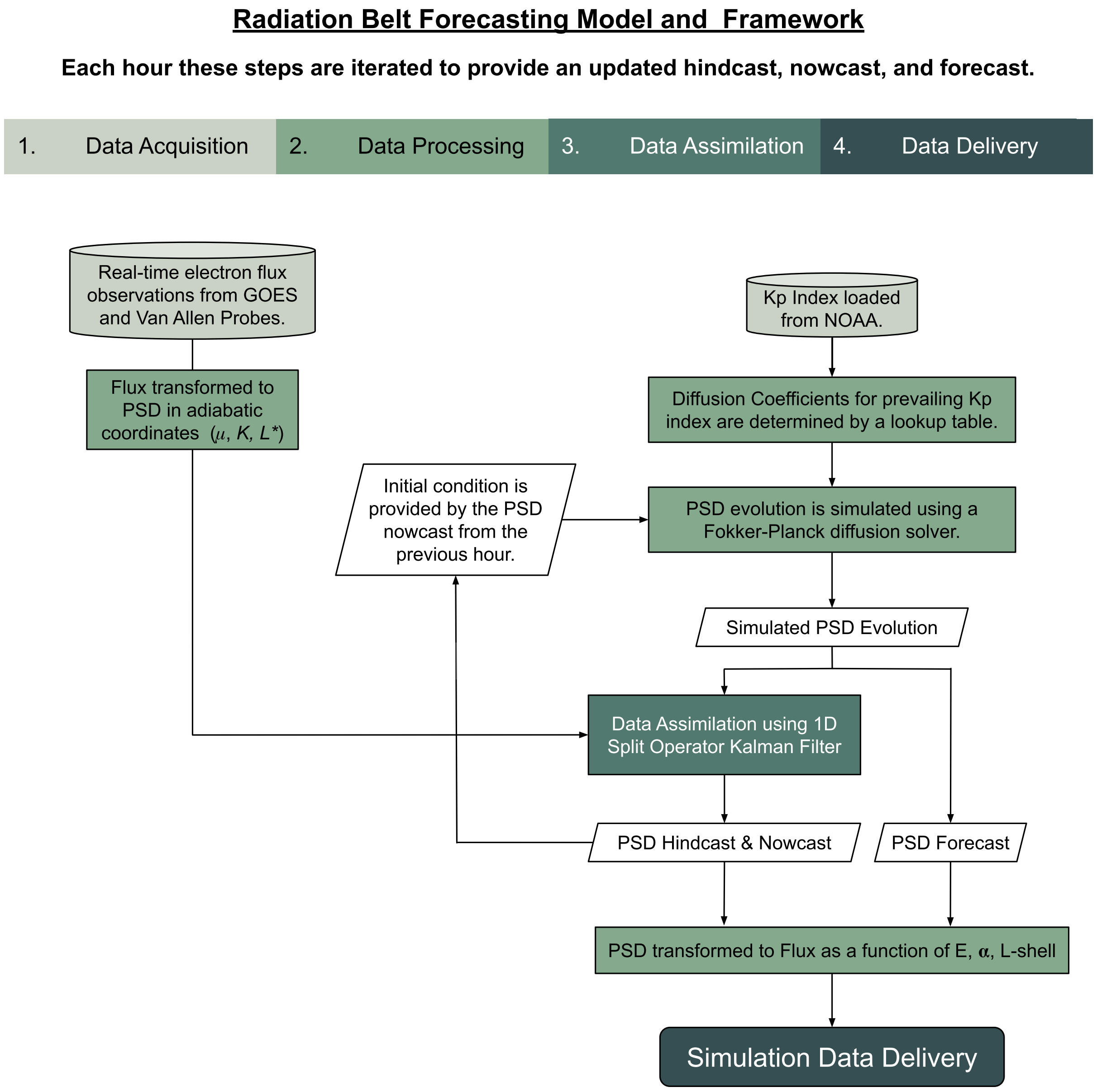

Figure 1. Flow chart summarizing the steps completed each hour in the Radiation Belt Forecasting Model and Framework.

Kellerman et al., 2014) to provide a robust infrastructure with data products which are integrated into the SatCAT tool. The implementation of this framework is summarized in Figure 1.

2.1. Diffusive Modeling

Radiation belt diffusion is modeled through implementation of the 3-D Fokker-Plank diffusion equation for radiation, Equation 1 (Roederer, 1970; Schulz & Lanzerotti, 1974; Walt, 1994). The Versatile Electron Radiation Belt code (Subbotin & Shprits, 2009) is used to implement a solution to this equation using precomputed diffusion coefficients.

$$\frac{\partial f}{\partial t} = \sum_{i,j} \frac{\partial}{\partial J_i}\left(D_{J_i J_j}\frac{\partial f}{\partial J_j}\right) - \text{Losses} \tag{1}$$

Where f is the phase averaged electron phase space density (PSD), J_i, J_j, represent the first, second, and third adiabatic invariants of adiabatic motion (μ, J, Φ respectively), and diffusion coefficients $D_{J_i J_j} = \langle \Delta J_i \Delta J_j \rangle / (2\,\Delta\, t)$ which denote the scattering rates ($D_{\mu\mu}, D_{JJ}, D_{\Phi\Phi}$). In this paper we use K ($K \propto J$ assuming μ is conserved) as the second adiabatic invariant and L^* ($L* \propto 1/\Phi$) as the third adiabatic invariant (noting that $L^* = L$ in a dipolar magnetic field).

2.1.1. Diffusion Coefficients

By precomputing diffusion matrices, the diffusion equation can be solved quickly at each time step by selecting diffusion coefficients for the prevailing *Kp* level. Mixed local diffusion terms are excluded, which enables larger grid steps. Three types of waves were used to derive the diffusion coefficient matrices; ULF waves (Brautigam & Albert, 2000), lower-band chorus (W. Li et al., 2007; Shprits et al., 2007) and plasmaspheric hiss (Spasojevic et al., 2015). The plasma density was obtained from (Sheeley et al., 2001) for diffusion coefficient computation. The diffusion coefficients were computed using the Full Diffusion Code at UCLA.

2.1.2. Initial and Boundary Conditions

Diffusion is solved for a dipolar magnetic field with a grid covering L-shells 1 to 7, energies 10 keV to 10 MeV, and pitch angles 0.3^{o}–89.7^{o}. The upper boundary condition in energy is a Dirichlet boundary with constant $f\ = 0$, the lower-boundary condition is also Dirichlet for each time step, although updated by assimilation. The lower boundary condition in pitch angle is a Neumann boundary $\partial f / \partial \alpha\ = 0$, to allow for both weak and strong diffusion effects to be simulated. The outer boundary condition at $L_{\text{max}} = 7$ is a Neumann boundary ($df / dL\ = 0$) when the last closed drift shell is outside the model domain >7 (LCDS; derived from Tsyganenko (1989) with a centered dipole, see Kellerman (2018) for more details). When the LCDS < 7 the outer boundary is set to a Dirichlet boundary ($f\ = 0$) to allow fast diffusion under compressed magnetospheric conditions. The lower boundary in L is also a Dirichlet boundary, with $f\ = 0$ at L_{min}, representing loss to the atmosphere.

The model was initialized through the average PSD observed by spacecraft from the previous month. For each additional forecast going forward through several years, the initial condition of each time step is set to the nowcast simulated for the previous hour.

2.2. Data Assimilation

Data assimilation uses filtering algorithms to estimate the state of a system using joint probability distributions from a simulated system and sparsely observed data. The Kalman Filter (Kalman, 1960) is a widely used data assimilation algorithm which estimates the system state by minimizing the mean square errors of the simulated state variables and observed state variables. Readers are referred to past works for descriptions of different Kalman filter methodologies used in radiation belt analysis (e.g., Castillo Tibocha et al., 2021; Kondrashov et al., 2007; Naehr & Toffoletto, 2005; Ni et al., 2009; Shprits et al., 2007).

Real-time satellite data was assimilated into RBFMF through a one-dimensional split-operator Kalman filtering algorithm, described in detail in Supporting Information S1, which was developed by Shprits et al. (2013). This methodology is computationally lightweight, making it practical for real-time applications, and has been validated in a synthetic-forecast analysis over multiple years (Kellerman et al., 2014; Shprits et al., 2013). In RBFMF the data assimilation model is "tuned" to consider observations with a greater weighting than the diffusive simulation by adjusting their respective errors. Errors are computed as $\left(Wx_f\right)^2$ where $W = 10$ for the diffusive simulation, and $W = 1$ for observations, and x_f describes the respective state vectors.

The RBFMF assimilates operational space weather data from the GOES and Van Allen Probe missions in real-time. The Van Allen Probe real-time data, or "beacon" data, was broadcast continuously at low data resolution to any receiver capable of receiving during periods where primary science data was not being downlinked, see Kessel et al. (2014) for full details of this data product. There are considerable differences between the Van Allen probe beacon data and final science data; there were large data gaps due to downlinking procedures, lower resolution in time and energy, and the beacon data did not undergo the same correction algorithms as the final science data (Baker et al., 2014; Blake et al., 2014; Claudepierre et al., 2015, 2021). Additionally, there are differences to the adiabatic coordinate calculation for both beacon data and real-time GOES data because the real-time Kp index was used as input for the T89 field model, whereas the definitive Kp index was used to process final science PSD data.

3. Validation Methodology

3.1. Multi-Mission PSD Observations

In this analysis, the RBFMF is validated against a multi-mission data set of radiation belt observations which serves as the "true" state of the radiation belt. We use a combined mission approach so that one mission does not overwhelmingly introduce a bias to the evaluation. PSD observations are taken from 32 individual satellites which are part of 5 different scientific missions and hosted payloads (see Staples et al., 2022, 2023 for further description of calibration and usage of this data set):

- Van Allen Probe Magnetic Electron Ion Spectrometer (MagEIS) and Relativistic Electron-Proton Telescope instruments (Baker et al., 2014; Blake et al., 2014; Claudepierre et al., 2021).
- GOES 13 and 15 (Geostationary Operational Environmental Satellite) Magnetospheric Electron Detector Energetic Proton, Electron, and Alpha Detector (Rodriguez, 2014a, 2014b; Sillanpää et al., 2017).
- Global Positioning System (GPS) Navstar Combined X-ray dosimeter (CXD) (Morley et al., 2016, 2017; Tuszewski et al., 2004).
- THEMIS (Time History of Events and Macroscale Interactions during Substorms) Electrostatic Analyzer (ESA) and Solid-State Telescope (SST) (Angelopoulos, 2008; Angelopoulos et al., 2008; McFadden et al., 2008).
- MMS (Magnetospheric Multiscale) Fly's Eye Electron Proton Spectrometer (FEEPS) (Blake et al., 2016; Burch et al., 2016).

All spacecraft data is calibrated to Van Allen Probe B MagEIS data. In addition, the calibrated GOES 15 data are used together with Van Allen Probe B as a baseline "gold standard" for all other the calibrations. Conjunctions between pairs of spacecraft are found within 10 min and 0.1 L^*, then a statistical correction is found for each instrument energy channel and PSD magnitude by numerically finding the best function to describe PSD offsets observed during conjunctions. The GPS pitch angle distributions are assumed using the Zhao et al. (2018) model. For each spacecraft instrument, the adiabatic invariants μ, K, and L^* are computed using a model magnetospheric field, represented by the International Geomagnetic Reference Field model (IGRF; Thébault et al., 2015) and Tsyganenko (1989) external magnetic field model (T89). The final PSD data set is interpolated across dimensions of μ and K to match the simulation coordinates, then PSD is averaged into L^* bins on an hourly basis to match the resolution of the RBFMF hindcast.

It is important to note that the test data set of Van Allen probe observations used to intercalibrate multi-mission data was considerably different to the real-time beacon data assimilated into RBFMF, as described in Section 2.2. However, we acknowledge that (uncalibrated) real-time GOES data was similar to final calibrated test data, so may not provide a reliable representation of model performance. Hence, the following analysis at geostationary orbits is supplemented by MMS and THEMIS observations.

3.2. Observations

Figure 2 shows how the modeled radiation belt PSD compares to the multi-mission PSD observations. The nowcast time is indicated in Figure 2 by the white line, with the preceding 8 days showing hindcast PSD, and the following 2 days show the PSD forecast. By comparing the modeled PSD in Figure 2a to the measured PSD in Figure 2b, we can see that the RBFMF is highly successful at reproducing the structure and dynamical evolution of the radiation belt in this example. The magnitude of the radiation belt flux is well captured overall, although when the observed PSD became enhanced up to $\sim 15 \times 10^{-5}$ $(\mathrm{c/cm/MeV})^3$ at $5 < L^* < 6$ between 6–9th August, the hindcast PSD appeared to be slightly underestimated. Figure 2c shows that the percentage error was <100% for most of the interval (i.e., PSD was estimated within a factor of 1 during the interval), but became largest (>200%) near the outer boundary ($L^* > 6$) as electrons were lost on 3rd August, and along the inner edge of the radiation belt ($4 < L^* < 5$) during the enhancement between 4th to 7th August.

While the interval in Figure 2 appears to show that the RBFMF is a good representation of the outer radiation belt, we must quantitatively evaluate the performance of the model to determine if it is accurate over long time periods, and identify when the simulation is inaccurate so that it can be improved. We tested the RBFMF against the

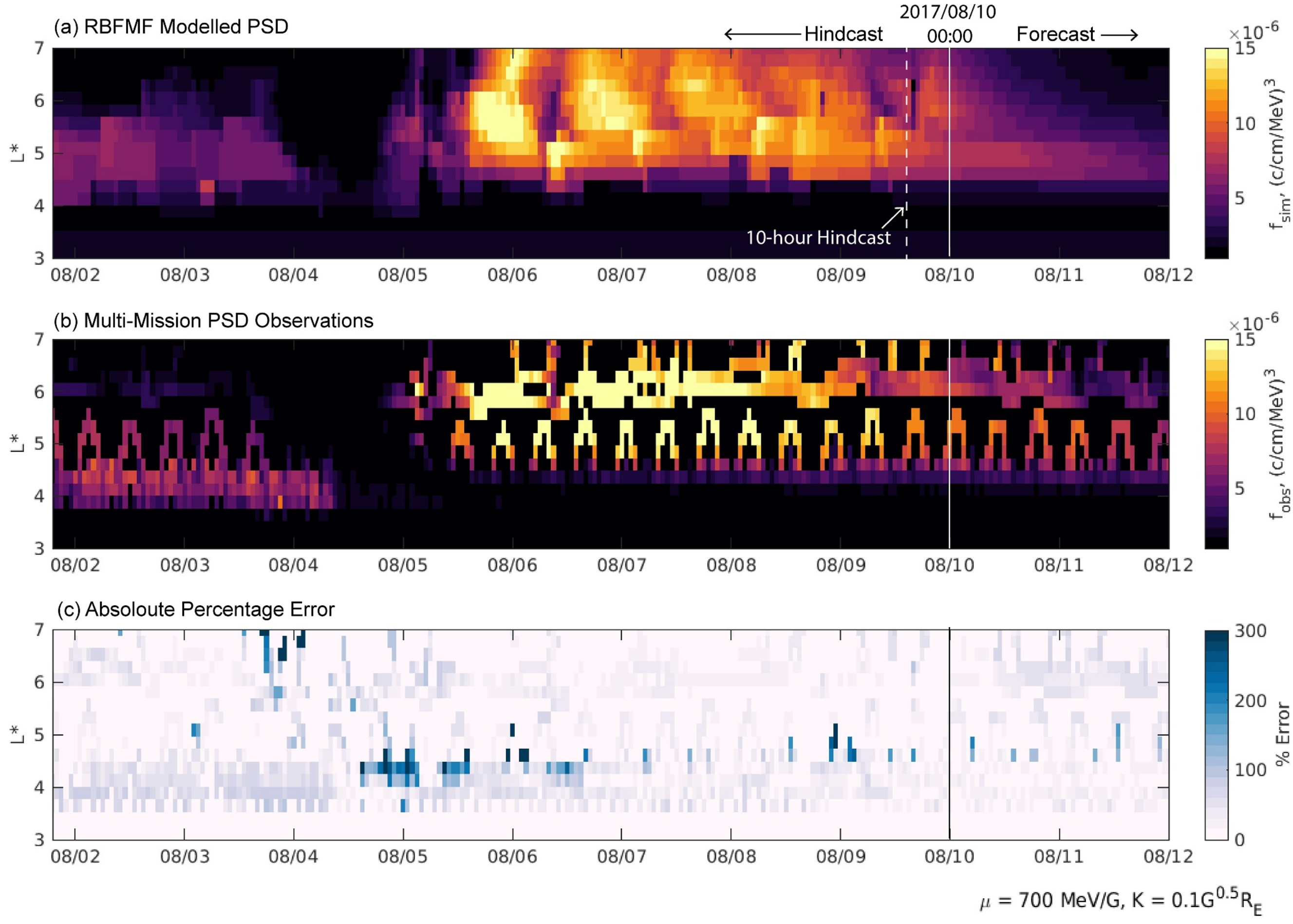

Figure 2. The simulated state of the radiation belt, f_{sim}, at 00 UT on 10 August 2017 is displayed in panel (a) as a function of L^* over time, for μ = 700 MeV/G and $K = 0.1$ G$^{0.5}$R$_E$. Panel (b) shows corresponding phase space densities observations, f_{obs}, taken by multiple missions. Panel (c) shows the absolute percentage error of the simulated PSD: $|f_{obs} - f_{sim}/f_{sim}| \times 100$.

observed state of the electron radiation belt for two time periods between 2016 and 2018 and between 2019 and 2020. The key difference between these years is that between 2016 and 2018 both GOES and Van Allen Probe beacon data were assimilated into the hindcast in real-time, whereas from 2019 onwards, only GOES data was assimilated in real-time.

3.3. Statistical Evaluation

The statistical error and bias of the 10-hr hindcast (dashed line, Figure 2a) is calculated between January 2016–October 2019 and between March 2019 and December 2020. For every PSD observation from the multi-mission data set, the quotient ($Q_i = f_{sim}/f_{obs}$) is calculated. Error and bias are quantified using symmetric metrics described by Morley et al. (2018), which account for variable electron PSD magnitudes. The median symmetric accuracy (MSA) is described in Equation 2 and the symmetric signed percentage bias (SSPB) is described in Equation 3, where M() symbolizes the median calculation. In this scheme, the MSA is small if simulation errors are low, SSPB < 0 if the hindcast is biased toward underprediction of PSD, and SSPB > 0 if the hindcast is biased toward overprediction of PSD.

$$\mathrm{MSA} = 100\left(\exp\left(\mathrm{M}(|\log_e(Q_i)|\right) - 1\right) \tag{2}$$

$$\mathrm{SSPB} = 100\,\mathrm{sgn}(M(\log_e(Q_i)))\left(\exp\left(\mathrm{M}(|\log_e(Q_i)|\right) - 1\right) \tag{3}$$

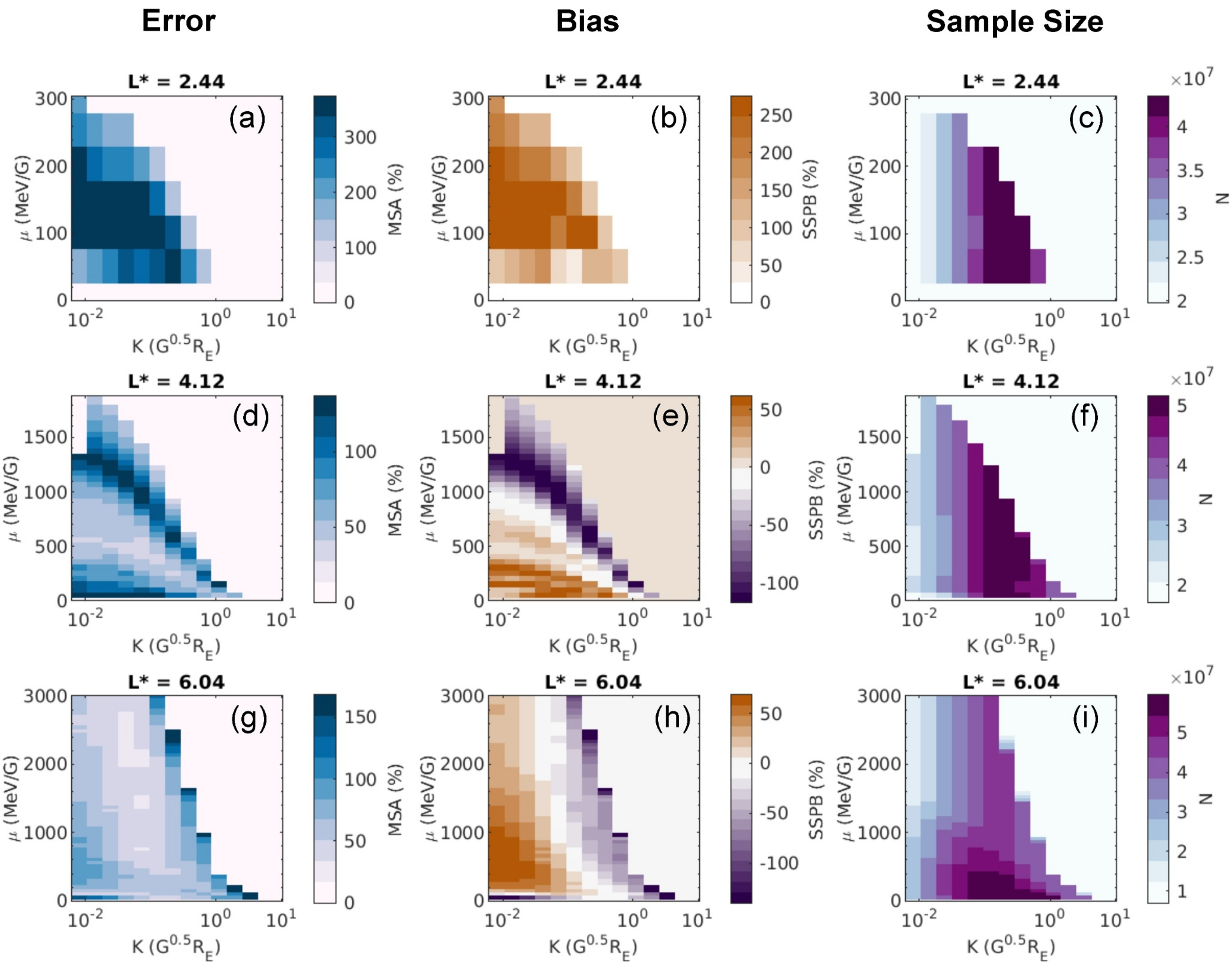

Figure 3. Left column shows the statistical error (median symmetric accuracy (MSA)) of the 10-hr hindcast between 2016 and 2018, shown by color as a function of μ and K for a sample of simulated $L* = 2.44$, 4.12, and 6.04. The middle column shows statistical bias (SSPB) in the same format, and right column shows the number of samples N used in the computation of MSA and SSPB.

4. Results

4.1. Original Forecast Framework (2016–2018)

Figure 3 shows the MSA, SSPB, and number of samples, N, calculated for the 10-hr hindcast of radiation belt PSD as a function of the first and second adiabatic invariants, μ and K at three sampled $L*$. The $L*$ values shown in Figure 3 are selected to represent trends in error and bias observed in the slot region ($\sim L* = 2.44$), the core of the outer radiation belt, and the outer radiation belt near medium earth orbit ($\sim L* = 4.12$) and at geostationary orbit ($\sim L* = 6.04$).

We observe a large variance in the MSA and SSBP across the different $L*$ regions. At $L* = 2.44$ the maximum percentage error was 350%, and the maximum bias was 250%. At $L* = 2.44$, electrons are generally located inside the overlapping plasmasphere and slot region, so the large positive bias indicates that the model systematically overestimated the PSD in the slot region. It is because electron PSD is generally very low at $L* < 4$, that comparatively small absolute differences in PSD create large errors and bias relative to the measured PSD.

In the outer radiation belt region ($L* > 4$) the error and bias were much smaller than the slot region, reaching a maximum of 150% percentage error and −150% bias. This indicates that statistically the hindcast accurately predicted the outer radiation belt PSD to within a factor of 1.5. Moreover, the hindcast error and bias was highly dependent upon μ and K.

At $L^* = 4.12$ the greatest errors were found to reach 150% corresponding to the highest measured μ values depending on K (i.e., highest energies, ~ multi-MeV) and was correspondingly biased toward underestimation of PSD by ~120%. At lower μ values (which correspond to the bulk of the radiation belt plasma population) the hindcast showed a statistical overestimation of PSD by 70% or less, showing that the hindcast predicted the core outer belt PSD to within a factor of 0.7. The hindcast error and bias showed similar trends at $L^* = 6.04$: The highest errors were observed at the highest measured μ (highest energies) with a negative bias $> -100\%$, and at lower μ the hindcast overestimated PSD by up to 70%. In addition to these error and bias relationships, at $L^* = 6.04$ there was a strong error of 150% and bias of −150% observed at $\mu < 100$ MeV/G. This population corresponds to lower energy <300 keV electron populations. To ensure that error and bias is not dependent upon hindcast hour, the same analysis was completed for different hindcast hour, and no appreciable differences were observed.

The following analysis discusses the source of the statistical hindcast error and bias and evaluates the accuracy of the hindcast under different geomagnetic conditions.

4.1.1. Assimilated Data Bias

One potential source of error in the modeled hindcast is a consistent bias of the assimilated real-time data used to drive the model relative to the more accurately post-processed data used for validation. Between 2016 and 2018 the assimilated data sets were real-time GOES data, and the Van Allen Probe Beacon data. The Van Allen Probe beacon data was provided in real-time over the Van Allen Probe mission without the same corrections and post-processing as the long-term science data archive, and so is possibly more prone to errors. To assess if the error and bias of assimilated PSD observations influenced the hindcast PSD, we evaluated the error and bias of the Van Allen Probe real-time Beacon data relative to the post-processed Van Allen Probe science data (Figure 4) and compared those results with the hindcast error and bias (Figure 3). The error and bias of Van Allen Probe beacon data is quantified by calculating the MSA and SSBP respectively using Equation 2 and Equation 3, where the quotient is calculated as $Q = \mathrm{PSD}_{\mathrm{Beacon}}/\mathrm{PSD}_{\mathrm{Final}}$, and $\mathrm{PSD}_{\mathrm{Final}}$ is the science data product from the same Van Allen Probe. This analysis effectively shows the differences between the real-time data product and the more highly processed science data as a function of μ, K, and L^*.

Figure 4 shows that the Van Allen Probe beacon data error and bias was greater than the 10-hr hindcast error and bias (Figure 3). For example, at $L^* = 2.44$, the error and bias of beacon data reached >800%, whereas the maximum hindcast error and bias were ~350% and ~250% respectively. What is more, the error and bias observed for beacon data (Figure 4) was nearly identically distributed across μ, K, and L^* compared to the hindcast error and bias. For example, at $L^* = 4.12$, the maximum errors were at the highest μ values across all K, and were negatively biased, transitioning to a positive bias at low μ values.

Because the error and bias of the hindcast shared the same relationship as the error and bias of beacon data, we conclude that hindcast error and bias between 2016 and 2019 was strongly influenced by error and bias in the assimilated Van Allen probe beacon data. The RBFMF simulation still provided a significantly improved estimate of radiation belt PSD compared to if Van Allen Probe beacon data were used alone since. As shown, the error and bias of the hindcast was much less than the assimilated data error and bias. Because the real-time GOES data is similar to the final science data product, it is not informative to conduct a similar evaluation of assimilated data errors.

4.1.2. Storm-Time Error Analysis

Knowing how well the model captures the radiation belt evolution during different geomagnetic conditions is of particular interest because most impacts to satellites are observed during geomagnetically active periods. To analyze how the statistical error and bias varies with geomagnetic conditions, we extract geomagnetic storm intervals between 2016 and 2018 based upon Sym-H index evolution. A storm is identified when Sym-H decreased to a minimum below −40 nT (to ensure that SIR driven storms were included; Grandin et al., 2019; Kilpua et al., 2015). The main storm phase is defined from Sym-H = 15 to the minimum Sym-H value, the recovery phase is defined from the minimum Sym-H to Sym-H = −15 nT. We further select times during

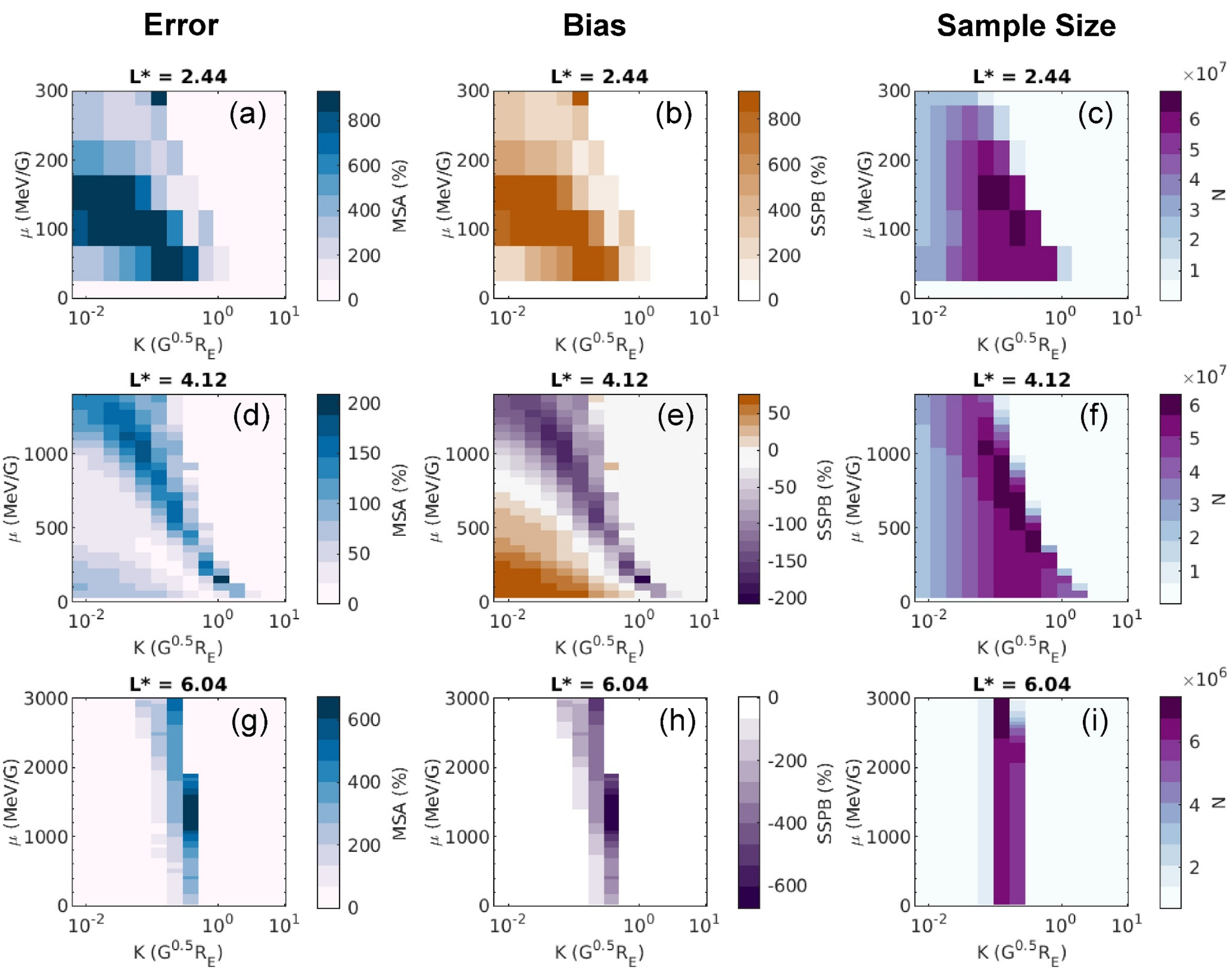

Figure 4. Left column shows the statistical error (median symmetric accuracy (MSA)) and middle column shows the statistical bias (SSPB) of the Van Allen Probe B beacon data between 2016 and 2018, compared to the final Van Allen Probe science data. Right column shows the number of data samples N used in the computation of MSA and SSPB. Error, bias, and sample size are all shown by color as a function of μ and K at sampled bins of $L^* = 2.44$; 4.12; 6.04 which were chosen to match the hindcast model grid.

geomagnetic storms when the AE index was in the upper 80% percentile of data. High AE index periods are known to be associated with substorm injections of lower energy source electrons from the magnetotail into the inner magnetosphere, and AE index values exceeding 150 nT have previously been used as a proxy for substorm injections (e.g., Meredith et al., 2000). As before, we calculate the statistical error and bias of each storm phase using Equations 2 and 3. Figures 5 and 6 show how the computed error and bias varied under different geomagnetic conditions at $L^* = 4.12$ and $L^* = 6.04$, respectively. To easily compare between geomagnetic conditions, the color bars have been saturated to ±200%. We do not show the equivalent figure for $L^* = 2.44$ as no substantial differences between storm phases were observed.

Figure 5 shows that the statistical error and bias under geomagnetically quiet conditions were effectively the same as for all data between 2016 and 2019 shown in Figure 3. This indicates that the overall statistical error and bias for the hindcast at $L^* = 4.12$ was not influenced by increased error or bias during geomagnetic variations. Figures 5g and 5h show that high μ values (highest energies $\geq$ MeV) appear least accurate and most biased during the recovery storm phase (and during substorm injections) as MSA increased to 200% at the highest μ values (panel g), and SSPB decreases to −200% (panel h). This indicates that, during the recovery phase, the hindcast underestimated the PSD of MeV electrons, which is understood to become enhanced during this phase (e.g., Jaynes et al., 2015; Murphy et al., 2018; Sorathia et al., 2018). Conversely, PSD of low μ electrons ($\lesssim$700 keV)

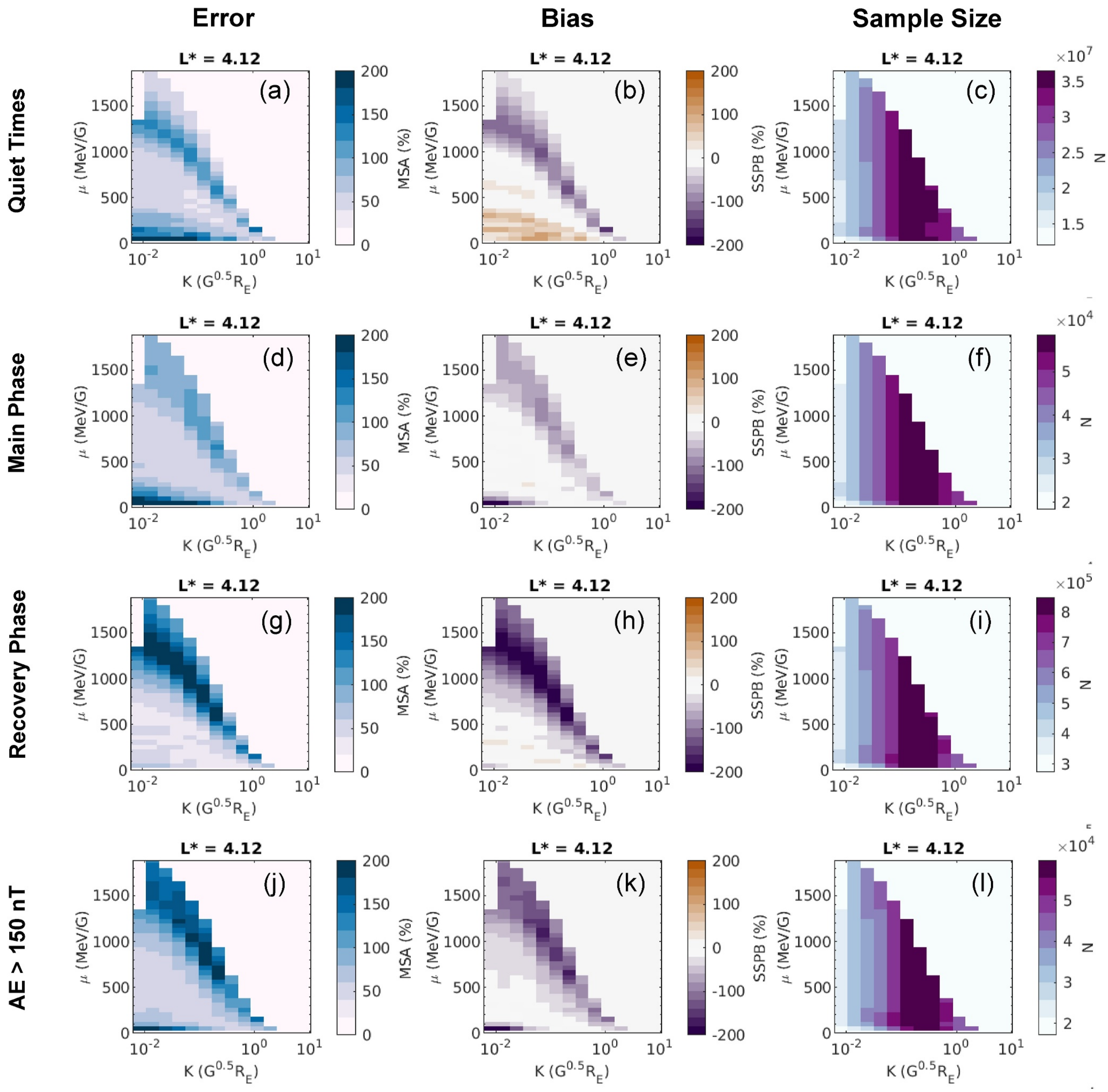

Figure 5. Left column shows the statistical error (median symmetric accuracy (MSA)) and middle column shows the statistical bias (SSPB) of the 10-hr hindcast between 2016 and 2018, compared to the final multi-mission phase space densities observations. Right column shows the number of data samples N used in the computation of MSA and SSPB. Error, bias, and sample size are all shown by color as a function of μ and K at sampled bins of $L^* = 4.12$. Each row shows error and bias under different geomagnetic conditions a–c are quiet times, d–f are the main storm phase, g–l are the recovery storm phase, and j–l show storm intervals where AE index >150 nT.

was less accurate during the main storm phase (panel d), and during substorm related injections (panel j–k). In both cases the error reached 200% and the hindcast was biased toward underestimation of PSD down to −200%. Figure 5 shows that the hindcast consistently underestimated PSD across all storm conditions at $L^* = 4.12$, for all μ and K.

Similarly, Figure 6 shows that at $L^* = 6.04$, quiet times exhibited the same statistical error and bias as the overall time period (Figure 3), and PSD of high μ (energies ≥ MeV) were the least accurate and most biased during the

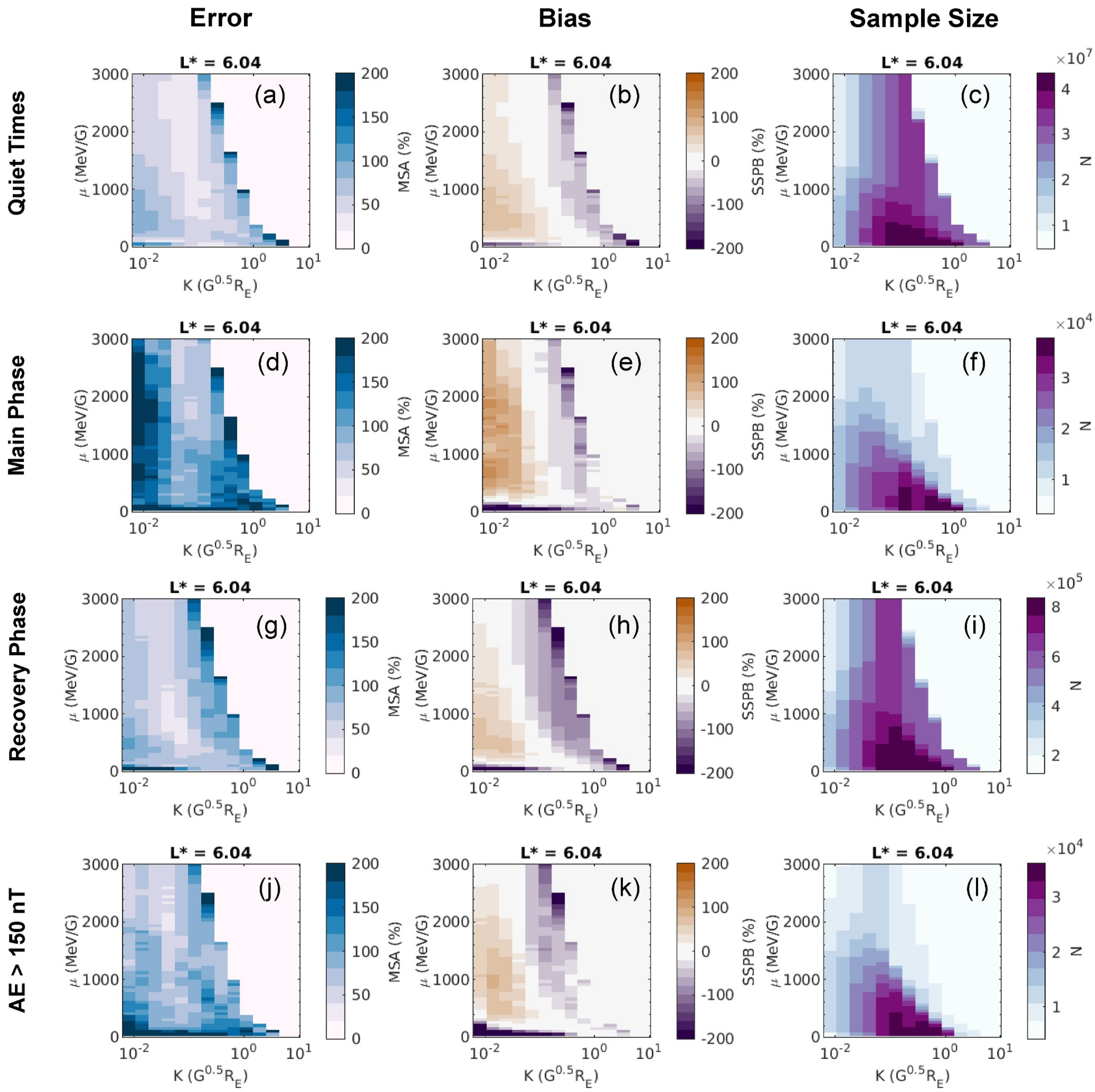

Figure 6. Statistical error and bias under different geomagnetic conditions, sampled at $L^* = 6.04$ is shown in the same format as Figure 5.

recovery phase of the storm (Figures 6g and 6h). Irrespective of μ However, Figure 6d shows that the largest overall errors were observed at low K (i.e., equatorial electrons) during the main storm phase. Given Figure 6e shows a bias toward overestimation of PSD at these K, and that $L^* = 6.04$ is near geostationary orbit, it is possible that loss to the outer boundary was not well captured by the hindcast. Figure 6j also shows large hindcast errors for $\mu < 500$ MeV/G, and bias toward underestimation of PSD by up to -200%. Since this feature was most prominent during storms with the highest AE index, we expect these errors were caused by substorm injections of lower-energy (<500 keV) electrons.

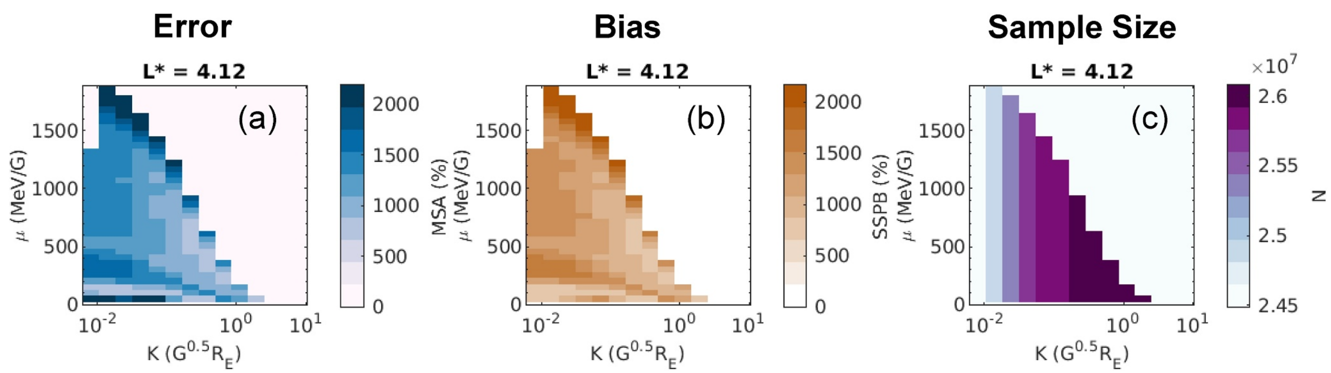

Figure 7. Statistical error (median symmetric accuracy, panel (a) and bias (symmetric signed percentage bias, panel (b) are of the 10-hr hindcast in 2019–2020 are shown as a function of μ and K at $L^* = 4.12$. The number of data samples, N, is shown in the panel (c).

4.2. Updated Forecast Framework (2019–2020)

Since the end of the Van Allen Probe mission in early 2019, the RBFMF has been operating by assimilating only GOES observations in real-time. To assess how this affected the accuracy of the 10-hr hindcast, we repeat the analysis presented in the previous section, comparing the 10-hr hindcast at $L^* = 4.2$ to PSD observations obtained from the GPS constellation between March 2019–December 2020 (Figure 7). Since the real-time GOES data assimilated into the hindcast model is similar to the final science data product, it is not meaningful to complete an error analysis at geostationary orbit using this data.

Figure 7 shows that the hindcast error and bias at $L^* = 4.12$ were significantly increased compared to the Van Allen Probe era (Figure 3), reaching maxima of >2,000%, which is a factor of 10 greater than was observed between 2016 and 2018. The hindcast was strongly biased toward overestimation of PSD at all μ and K values by similar magnitudes to the error, which suggests that the model could be improved by the inclusion of a corrective factor. It is important to note that GPS satellites do not resolve electron flux by pitch angle, so an assumed pitch angle distribution is used to calculate PSD as a function of μ, K, and L^*. It is possible that error and bias determined at $L^* = 4.12$ were affected by the uncertainty of the assumed pitch angle distribution used in GPS data processing, rather than actual errors in the hindcast.

We emphasize that the diffusive simulation driving the hindcast provided a good first approximation of radiation belt dynamics, but is somewhat rudimentary as simplified diffusive modeling was employed. However, we chose not to modify the forecast model until a comprehensive analysis of hindcast performance was conducted. Since less observational data is now available to constrain the hindcast via data assimilation, the diffusion simulation should be improved by updating the precomputed diffusion coefficients using more modern methodologies of representing Chorus (e.g., Wong et al., 2024), Hiss (e.g., Agapitov et al., 2020; Watt et al., 2019), and ULF waves (e.g., Murphy et al., 2023). The diffusive effects of EMIC waves could also be incorporated (e.g., Ross et al., 2020) to improve the representation of electron loss in the inner magnetosphere.

5. Summary

We have conducted a comprehensive assessment of the accuracy and bias of the RBFMF, which is used to specify the real-time radiation environment in the SatCAT. Historical hindcasts were compared to observations of the radiation belt by computing the statistical errors and bias between the years January 2016–October 2018 while the Van Allen Probes remained in operation, and between March 2019–December 2020 following the end of the Van Allen Probe mission.

The hindcast was found to be accurate to within a factor of 1.5 in the outer radiation belt ($4 < L^* < 7$) during the years when the Van Allen Probe data was assimilated into the model (Figures 3d and 3g). We identified that the statistical hindcast bias was predominantly introduced by the assimilated Van Allen Probe beacon data, which displayed the same dependence of bias upon μ and K (Figure 4). Analysis of geomagnetic storms between 2016 and 2018 also revealed increased hindcast error and bias compared to quiet times at $L^* > 4$. The most energetic electrons (>MeV) were more likely to be underestimated by the hindcast during storm recovery phase (Figure 5), error increased for equatorial electrons at $L^* \sim 6$ during the main storm phase (Figure 6d), and the hindcast underestimated lower energy electrons (<500 keV) related to substorm injections (Figure 6j).

We have shown that the hindcast was much more accurate at predicting PSD than if the Van Allen Probe beacon data was used alone (Figure 4). Moreover, we found that the Van Allen Probe beacon data played a crucial role in constraining hindcast simulation between 2016 and 2019 as the hindcast error and bias increased tenfold at $L^* = 4.1$ when the Van Allen Probe data was no longer assimilated (2018–2020). This highlights that combining pre-processed data with physics-based modeling through data assimilation can improve the accuracy of radiation environment specification than either method used alone.

6. Future Work

Our analysis has emphasized the importance of real-time observations at multiple locations through the outer radiation belt. Even though the beacon Van Allen Probe data contained significant error and bias compared to the final processed data, assimilation of these observations into the RBFMF considerably improved the simulation compared to times where it was not assimilated. Furthermore, we showed that data assimilative techniques displayed less error and bias than pre-processed/low resolution real-time observations when the two were compared to final processed science data. Since the end of the Van Allen Probe mission, there are no similar observations available as the currently operational observatories (e.g., GPS, ARASE) do not provide publicly available data in real-time. We emphasize that any provision of real-time observations from existing or new missions enhance the operational impact of data, even if it is sub-optimally processed compared to science quality data. Furthermore, analysis of real-time data errors, analogous to our analysis of beacon Van Allen Probe data, can be used to inform the observational uncertainties used during data assimilation simulations.

In lieu of real-time observations to constrain this stimulation through the heart of the radiation belt, there is much scope to develop the physics simulation to improve hindcast performance using only GOES data inputs. For example, Glauert et al. (2018) demonstrated that the BAS-RBM model (Glauert et al., 2014) can achieve high performance levels (SSPB <138%) when >2 MeV GOES observations were used to define the outer boundary of their simulation.

Our analysis has highlighted key areas in which the physics simulation used in RBFMF could be improved. Overestimation of PSD in the plasmasphere could be addressed by evaluating more recent diffusion coefficients computed for Plasmaspheric Hiss (e.g., Agapitov et al., 2020; Watt et al., 2019). Improved representation of electron loss at geostationary orbit during the storm main phase could be incorporated by using a dynamic outer boundary of the simulation (Bloch et al., 2021; Staples et al., 2020) and evaluating new radial diffusion coefficients (Murphy et al., 2023). Updating the radial diffusion coefficients could also improve hindcast with sparse real-time data by accurately propagating the effects of assimilated data across L^*. Underestimation of ultra-relativistic electrons during the storm recovery phase could be improved by updating energy diffusion through new parameterizations of Chorus waves (e.g., Wong et al., 2024). Furthermore, substorm injections of lower energy electrons are necessary, and could be incorporated through updates to the simulation boundaries.

At time of publication, the RBFMF remains in operation using GOES observations as real-time inputs, producing radiation belt specifications for the SatCAT tool. Our investigation revealed that significant development is needed to improve the hindcast in locations where data is no longer assimilated. Continued development of the physics-based simulation is ongoing so that new versions of the RBFMF can deliver improved hindcast accuracy. Our analysis of RBFMF error and bias provides a crucial baseline to measure improvements to radiation belt hindcast specification.

Data Availability Statement

Spacecraft data from GOES, MMS, THEMIS, and the Van Allen Probes are publicly available via the NASA/GSFC CDAWeb service (NASA, 2024a). Solar Wind data and Sym-H index are publicly available through the NASA/GSFC Space Physics Data Facility OMNIWeb service (NASA, 2024b) and Kp index is available via Matzka (2021). The LANL-GPS particle data are publicly available via NOAA (2021). Processed 10-hr hindcast data, multi-mission phase space density data, and Van Allen Probe beacon data used in this manuscript is publicly available via Kellerman and Staples (2024). We acknowledge the use of the IRBEM library (version v5.0.0), the latest version of which is published on GitHub (Boscher et al., 2022).

Acknowledgments
FS and ACK acknowledge support from NASA Grants 80NSSC20K1402 and 80NSSC23K0096 and NSF Grant 2149782, and JG acknowledges acknowledge support from NASA Grant 80NSSC20K1402 and NSF Grant 2149782. We gratefully acknowledge the dedicated mission teams involved development of many data sets used in this work: The NASA Van Allen Probes and Harlan E. Spence for use of their data. The CXD team at Los Alamos National Laboratory which designed and built the CXD and BDD-IIR instruments discussed in this article. The entire MMS mission team, including development, science operations, and the Science Data Center at the Univ. of Colorado. We especially benefitted from the efforts of Ian Cohen and Christine Gabrielse for their advice on FEEPS data processing. We acknowledge NASA contract NAS5-02099 and V. Angelopoulos for use of data from the THEMIS Mission, specifically: D. Larson and the late R. P. Lin for use of SST data. The National Oceanic and Atmosphere Administration for real-time data from the GOES satellites. We gratefully acknowledge the NOAA Space Weather Prediction Center for providing computations of the 3-day Kp-index forecast, and the magnetometer data providers around the world, including the U.S. Geological Survey, Natural Resources Canada (NRCAN), the British Geological Survey, the German Research Centre for Geosciences (GFZ), and Geoscience Australia.

References

Agapitov, O., Mourenas, D., Artemyev, A., Claudepierre, S. G., Hospodarsky, G., & Bonnell, J. W. (2020). Lifetimes of relativistic electrons as determined from plasmaspheric hiss scattering rates statistics: Effects of ω_{pe}/Ω_{ce} and wave frequency dependence on geomagnetic activity. *Geophysical Research Letters*, *47*(13), e2020GL088052. https://doi.org/10.1029/2020GL088052

Angelopoulos, V. (2008). The THEMIS mission. *Space Science Reviews*, *141*(1), 5–34. https://doi.org/10.1007/s11214-008-9336-1

Angelopoulos, V., Sibeck, D., Carlson, C. W., McFadden, J. P., Larson, D., Lin, R. P., et al. (2008). First results from the THEMIS mission. *Space Science Reviews*, *141*(1), 453–476. https://doi.org/10.1007/s11214-008-9378-4

Baker, D. N., Kanekal, S. G., Hoxie, V. C., Batiste, S., Bolton, M., Li, X., et al. (2014). The relativistic electron-proton telescope (REPT) instrument on board the radiation belt storm probes (RBSP) spacecraft: Characterization of Earth's radiation belt high-energy particle populations. In N. Fox & J. L. Burch (Eds.), *The Van Allen probes mission* (pp. 337–381). Springer US.

Blake, J. B., Carranza, P. A., Claudepierre, S. G., Clemmons, J. H., Crain, W. R., Dotan, Y., et al. (2014). The magnetic electron ion spectrometer (MagEIS) instruments aboard the radiation belt storm probes (RBSP) spacecraft. In N. Fox & J. L. Burch (Eds.), *The Van Allen probes mission* (pp. 383–421). Springer US.

Blake, J. B., Mauk, B. H., Baker, D. N., Carranza, P., Clemmons, J. H., Craft, J., et al. (2016). The fly's eye energetic particle spectrometer (FEEPS) sensors for the magnetospheric multiscale (MMS) mission. *Space Science Reviews*, *199*(1–4), 309–329. https://doi.org/10.1007/s11214-015-0163-x

Bloch, T., Watt, C. E. J., Owens, M. J., Thompson, R. L., & Agiwal, O. (2021). Constraining the location of the outer boundary of Earth's outer radiation belt. *Earth and Space Science*, *8*(6), e2020EA001610. https://doi.org/10.1029/2020EA001610

Boscher, D., Bourdarie, S., O'Brien, P., Guild, T., Heynderickx, D., Morley, S., et al. (2022). The international radiation belt environment modeling library (PRBEM/IRBEM): v5.0.0 [Software]. https://github.com/PRBEM/IRBEM/releases

Bourdarie, S. A., & Maget, V. F. (2012). Electron radiation belt data assimilation with an ensemble Kalman filter relying on the Salammbô code. *Annals of Geophysics*, *30*(6), 929–943. https://doi.org/10.5194/angeo-30-929-2012

Boyd, A. J., Green, J. C., O'Brien, T. P., & Claudepierre, S. G. (2023). Specifying high altitude electrons using low-altitude LEO systems: Updates to the SHELLS model. *Space Weather*, *21*(3), e2022SW003338. https://doi.org/10.1029/2022SW003338

Brautigam, D. H., & Albert, J. M. (2000). Radial diffusion analysis of outer radiation belt electrons during the October 9, 1990, magnetic storm. *Journal of Geophysical Research*, *105*(A1), 291–309. https://doi.org/10.1029/1999JA900344

Brunet, A., Dahmen, N., Katsavrias, C., Santolík, O., Bernoux, G., Pierrard, V., et al. (2023). Improving the electron radiation belt nowcast and forecast using the SafeSpace data assimilation modeling pipeline. *Space Weather*, *21*(8), e2022SW003377. https://doi.org/10.1029/2022SW003377

Burch, J. L., Moore, T. E., Torbert, R. B., & Giles, B. L. (2016). Magnetospheric multiscale overview and science objectives. *Space Science Reviews*, *199*(1), 5–21. https://doi.org/10.1007/s11214-015-0164-9

Camporeale, E. (2019). The challenge of machine learning in space weather: Nowcasting and forecasting. *Space Weather*, *17*(8), 1166–1207. https://doi.org/10.1029/2018SW002061

Castillo Tibocha, A. M., de Wiljes, J., Shprits, Y. Y., & Aseev, N. A. (2021). Reconstructing the dynamics of the outer electron radiation belt by means of the standard and ensemble Kalman filter with the VERB-3D code. *Space Weather*, *19*(10), e2020SW002672. https://doi.org/10.1029/2020SW002672

Chen, Y., Reeves, G. D., Fu, X., & Henderson, M. (2019). PreMevE: New predictive model for megaelectron-volt electrons inside Earth's outer radiation belt. *Space Weather*, *17*(3), 438–454. https://doi.org/10.1029/2018SW002095

Claudepierre, S. G., Blake, J. B., Boyd, A. J., Clemmons, J. H., Fennell, J. F., Gabrielse, C., et al. (2021). The magnetic electron Ion spectrometer: A review of on-orbit sensor performance, data, operations, and science. *Space Science Reviews*, *217*(8), 80. https://doi.org/10.1007/s11214-021-00855-2

Claudepierre, S. G., O'Brien, T. P., Blake, J. B., Fennell, J. F., Roeder, J. L., Clemmons, J. H., et al. (2015). A background correction algorithm for Van Allen Probes MagEIS electron flux measurements. *Journal of Geophysical Research: Space Physics*, *120*(7), 5703–5727. https://doi.org/10.1002/2015JA021171

Coleman, T., McCollough, J. P., Young, S., & Rigler, E. J. (2018). Operational nowcasting of electron flux levels in the outer zone of Earth's radiation belt. *Space Weather*, *16*(5), 501–518. https://doi.org/10.1029/2017SW001788

Daae, M., Shprits, Y. Y., Ni, B., Koller, J., Kondrashov, D., & Chen, Y. (2011). Reanalysis of radiation belt electron phase space density using various boundary conditions and loss models. *Advances in Space Research*, *48*(8), 1327–1334. https://doi.org/10.1016/j.asr.2011.07.001

du Montcel, B. t. T., Trouche, A., Michaelis, I., Jeanty-Ruard, B., Wutzig, M., Forest, J., & Shprits, Y. Y. (2023). Presentation and validation of the internal charging risk forecast in the PAGER framework. *Advances in Space Research*, *72*(9), 3666–3676. https://doi.org/10.1016/j.asr.2023.07.047

Fennell, J. F., Koons, H. C., Roeder, J. L., & Blake, J. B. (2001). Spacecraft charging: Observations and relationship to satellite anomalies. Spacecraft Charging Technology. In *Proceedings of the Seventh International Conference* (pp. 279–284). European Space Agency Special Publication. *ESA SP-476*.

Gabrielse, C., Lee, J. H., Claudepierre, S., Walker, D., O'Brien, P., Roeder, J., et al. (2022). Radiation belt daily average electron flux model (RB-Daily-E) from the seven-year Van Allen probes mission and its application to interpret GPS on-orbit solar array degradation. *Space Weather*, *20*(11), e2022SW003183. https://doi.org/10.1029/2022SW003183

Galvan, D. A., Hemenway, B., Welser, W., & Baiocchi, D. (2014). *Satellite anomalies benefits of a centralized anomaly database and methods for securely sharing information among satellite operators*. RAND Corporation.

Glauert, S. A., Horne, R. B., & Meredith, N. P. (2014). Three-dimensional electron radiation belt simulations using the BAS Radiation Belt Model with new diffusion models for chorus, plasmaspheric hiss, and lightning-generated whistlers. *Journal of Geophysical Research: Space Physics*, *119*(1), 268–289. https://doi.org/10.1002/2013JA019281

Glauert, S. A., Horne, R. B., & Meredith, N. P. (2018). A 30-year simulation of the outer electron radiation belt. *Space Weather*, *16*(10), 1498–1522. https://doi.org/10.1029/2018SW001981

Grandin, M., Aikio, A. T., & Kozlovsky, A. (2019). Properties and geoeffectiveness of solar wind high-speed streams and stream interaction regions during solar cycles 23 and 24. *Journal of Geophysical Research: Space Physics*, *124*(6), 3871–3892. https://doi.org/10.1029/2018JA026396

Green, J. C., Likar, J., & Shprits, Y. (2017). Impact of space weather on the satellite industry. *Space Weather*, *15*(6), 804–818. https://doi.org/10.1002/2017SW001646

Green, J. C., Quinn, R., O'Brien, T. P., Likar, J., Shprits, Y., Boyd, A. J., et al. (2020). Developing a comprehensive application for satellite anomaly analysis and attribution. In *Paper presented at the Advanced Maui Optical and Space Surveillance Technologies Conference (AMOS)*.

Horne, R. B., Glauert, S. A., Meredith, N. P., Boscher, D., Maget, V., Heynderickx, D., & Pitchford, D. (2013). Space weather impacts on satellites and forecasting the Earth's electron radiation belts with SPACECAST. *Space Weather*, *11*(4), 169–186. https://doi.org/10.1002/swe.20023

Jaynes, A. N., Baker, D. N., Singer, H. J., Rodriguez, J. V., Loto'aniu, T. M., Ali, A. F., et al. (2015). Source and seed populations for relativistic electrons: Their roles in radiation belt changes. *Journal of Geophysical Research: Space Physics*, *120*(9), 7240–7254. https://doi.org/10.1002/2015JA021234

Kalman, R. E. (1960). A new approach to linear filtering and prediction problems. *Journal of Basic Engineering*, *82*(1), 35–45. https://doi.org/10.1115/1.3662552

Kellerman, A. C. (2018). Chapter 10 - Prediction of MeV electron fluxes and forecast verification. In E. Camporeale, S. Wing, & J. R. Johnson (Eds.), *Machine learning techniques for space weather* (pp. 259–278). Elsevier.

Kellerman, A. C., Shprits, Y. Y., Kondrashov, D., Subbotin, D., Makarevich, R. A., Donovan, E., & Nagai, T. (2014). Three-dimensional data assimilation and reanalysis of radiation belt electrons: Observations of a four-zone structure using five spacecraft and the VERB code. *Journal of Geophysical Research: Space Physics*, *119*(11), 8764–8783. https://doi.org/10.1002/2014JA020171

Kellerman, A. C., & Staples, F. A. (2024). Radiation belt forecast model and framework (RBFMF) 10 hour hindcast validation data. https://doi.org/10.5281/zenodo.11111470

Kessel, R. L., Fox, N. J., & Weiss, M. (2014). The radiation belt storm probes (RBSP) and space weather. In N. Fox & J. L. Burch (Eds.), *The Van Allen probes mission* (pp. 531–543). Springer US.

Kilpua, E. K. J., Hietala, H., Turner, D. L., Koskinen, H. E. J., Pulkkinen, T. I., Rodriguez, J. V., et al. (2015). Unraveling the drivers of the storm time radiation belt response. *Geophysical Research Letters*, *42*(9), 3076–3084. https://doi.org/10.1002/2015GL063542

Kondrashov, D., Shprits, Y., Ghil, M., & Thorne, R. (2007). A Kalman filter technique to estimate relativistic electron lifetimes in the outer radiation belt. *Journal of Geophysical Research*, *112*(A10). https://doi.org/10.1029/2007JA012583

Koons, H., Mazur, J., Selesnick, R., Blake, J., Fennell, J., Roeder, J., & Anderson, P. (1999). *The impact of the space environment on space systems* (pp. 69036–69041). NASA STI/Recon Technical Report N.

Li, W., Shprits, Y. Y., & Thorne, R. M. (2007). Dynamic evolution of energetic outer zone electrons due to wave-particle interactions during storms. *Journal of Geophysical Research*, *112*(A10). https://doi.org/10.1029/2007JA012368

Li, X. (2004). Variations of 0.7–6.0 MeV electrons at geosynchronous orbit as a function of solar wind. *Space Weather*, *2*(3). https://doi.org/10.1029/2003SW000017

Lohmeyer, W., Carlton, A., Wong, F., Bodeau, M., Kennedy, A., & Cahoy, K. (2015). Response of geostationary communications satellite solid-state power amplifiers to high-energy electron fluence. *Space Weather*, *13*(5), 298–315. https://doi.org/10.1002/2014SW001147

Matzka, J. B., Oliver, Tornow, K., Elger, K., & Stolle, C. (2021). Geomagnetic Kp index V. 1.0. [Dataset]. https://doi.org/10.5880/Kp.0001

McFadden, J. P., Carlson, C. W., Larson, D., Ludlam, M., Abiad, R., Elliott, B., et al. (2008). The THEMIS ESA plasma instrument and in-flight calibration. *Space Science Reviews*, *141*(1), 277–302. https://doi.org/10.1007/s11214-008-9440-2

Meredith, N. P., Horne, R. B., Johnstone, A. D., & Anderson, R. R. (2000). The temporal evolution of electron distributions and associated wave activity following substorm injections in the inner magnetosphere. *Journal of Geophysical Research*, *105*(A6), 12907–12917. https://doi.org/10.1029/2000JA900010

Morley, S. K., Brito, T. V., & Welling, D. T. (2018). Measures of model performance based on the log accuracy ratio. *Space Weather*, *16*(1), 69–88. https://doi.org/10.1002/2017SW001669

Morley, S. K., Sullivan, J. P., Carver, M. R., Kippen, R. M., Friedel, R. H. W., Reeves, G. D., & Henderson, M. G. (2017). Energetic particle data from the global positioning system constellation. *Space Weather*, *15*(2), 283–289. https://doi.org/10.1002/2017SW001604

Morley, S. K., Sullivan, J. P., Henderson, M. G., Blake, J. B., & Baker, D. N. (2016). The Global Positioning System constellation as a space weather monitor: Comparison of electron measurements with Van Allen Probes data. *Space Weather*, *14*(2), 76–92. https://doi.org/10.1002/2015SW001339

Murphy, K. R., Sandhu, J., Rae, I. J., Daggitt, T., Glauert, S., Horne, R. B., et al. (2023). A new four-component L*-Dependent model for radial diffusion based on solar wind and magnetospheric drivers of ULF waves. *Space Weather*, *21*(7), e2023SW003440. https://doi.org/10.1029/2023SW003440

Murphy, K. R., Watt, C. E. J., Mann, I. R., Jonathan Rae, I., Sibeck, D. G., Boyd, A. J., et al. (2018). The global statistical response of the outer radiation belt during geomagnetic storms. *Geophysical Research Letters*, *45*(9), 3783–3792. https://doi.org/10.1002/2017GL076674

Naehr, S. M., & Toffoletto, F. R. (2005). Radiation belt data assimilation with an extended Kalman filter. *Space Weather*, *3*(6). https://doi.org/10.1029/2004SW000121

Nagai, T. (1988). "Space weather forecast": Prediction of relativistic electron intensity at synchronous orbit. *Geophysical Research Letters*, *15*(5), 425–428. https://doi.org/10.1029/GL015i005p00425

NASA. (2024a). CDAWeb [Dataset]. Goddard Space Flight Center Space Physics Data Facility. https://cdaweb.gsfc.nasa.gov/index.html/

NASA. (2024b). OMNIWeb plus [Dataset]. from Goddard Space Flight Center Space Physics Data Facility. https://omniweb.gsfc.nasa.gov/

Ni, B., Shprits, Y., Nagai, T., Thorne, R., Chen, Y., Kondrashov, D., & Kim, H.-j. (2009). Reanalyses of the radiation belt electron phase space density using nearly equatorial CRRES and polar-orbiting Akebono satellite observations. *Journal of Geophysical Research*, *114*(A5). https://doi.org/10.1029/2008JA013933

NOAA. (2021). GPS energetic charged particle data product files V1.03 [Dataset]. NOAA's National Centers for Environmental Information. http://www.ngdc.noaa.gov/stp/space-weather/satellite-data/satellite-systems/gps/

Rodriguez, J. V. (2014a). GOES 13-15 MAGE/PD pitch angles algorithm theoretical basis document. Retrieved from https://ngdc.noaa.gov/stp/satellite/goes/documentation.html

Rodriguez, J. V. (2014b). GOES EPEAD science-quality electron fluxes algorithm theoretical basis document. Retrieved from https://ngdc.noaa.gov/stp/satellite/goes/doc/EPEAD_Electron_Science_Reprocessing_ATBD_v1.0.pdf

Roeder, J. L., Chen, M. W., Fennell, J. F., & Friedel, R. (2005). Empirical models of the low-energy plasma in the inner magnetosphere. *Space Weather*, *3*(12). https://doi.org/10.1029/2005SW000161

Roederer, J. (1970). Dynamics of geomagnetically trapped radiation, phys. and chem. *Space*, *2*, 166.

Ross, J. P. J., Glauert, S. A., Horne, R. B., Watt, C. E., Meredith, N. P., & Woodfield, E. E. (2020). A new approach to constructing models of electron diffusion by EMIC waves in the radiation belts. *Geophysical Research Letters*, *47*(20), e2020GL088976. https://doi.org/10.1029/2020GL088976

Schulz, M., & Lanzerotti, L. J. (1974). Particle diffusion in the radiation belts. *Physics and Chemistry in Space*.

Sheeley, B. W., Moldwin, M. B., Rassoul, H. K., & Anderson, R. R. (2001). An empirical plasmasphere and trough density model: CRRES observations. *Journal of Geophysical Research*, *106*(A11), 25631–25641. https://doi.org/10.1029/2000JA000286

Shin, D.-K., Lee, D.-Y., Kim, K.-C., Hwang, J., & Kim, J. (2016). Artificial neural network prediction model for geosynchronous electron fluxes: Dependence on satellite position and particle energy. *Space Weather*, *14*(4), 313–321. https://doi.org/10.1002/2015SW001359

Shprits, Y., Kellerman, A., Kondrashov, D., & Subbotin, D. (2013). Application of a new data operator-splitting data assimilation technique to the 3-D VERB diffusion code and CRRES measurements. *Geophysical Research Letters*, *40*(19), 4998–5002. https://doi.org/10.1002/grl.50969

Shprits, Y., Kondrashov, D., Chen, Y., Thorne, R., Ghil, M., Friedel, R., & Reeves, G. (2007). Reanalysis of relativistic radiation belt electron fluxes using CRRES satellite data, a radial diffusion model, and a Kalman filter. *Journal of Geophysical Research*, *112*(A12). https://doi.org/10.1029/2007JA012579

Sillanpää, I., Ganushkina, N. Y., Dubyagin, S., & Rodriguez, J. V. (2017). Electron fluxes at geostationary orbit from GOES MAGED data. *Space Weather*, *15*(12), 1602–1614. https://doi.org/10.1002/2017SW001698

Sorathia, K. A., Ukhorskiy, A. Y., Merkin, V. G., Fennell, J. F., & Claudepierre, S. G. (2018). Modeling the depletion and recovery of the outer radiation belt during a geomagnetic storm: Combined MHD and test particle simulations. *Journal of Geophysical Research: Space Physics*, *123*(7), 5590–5609. https://doi.org/10.1029/2018JA025506

Spasojevic, M., Shprits, Y. Y., & Orlova, K. (2015). Global empirical models of plasmaspheric hiss using Van Allen Probes. *Journal of Geophysical Research: Space Physics*, *120*(12), 10370–310383. https://doi.org/10.1002/2015JA021803

Staples, F. A., Kellerman, A., Murphy, K. R., Rae, I. J., Sandhu, J. K., & Forsyth, C. (2022). Resolving magnetopause shadowing using multimission measurements of phase space density. *Journal of Geophysical Research: Space Physics*, *127*(2), e2021JA029298. https://doi.org/10.1029/2021JA029298

Staples, F. A., Ma, Q., Kellerman, A., Rae, I. J., Sandhu, J. K., Forsyth, C., & Bortnik, J. (2023). Differentiating between simultaneous loss drivers in Earth's outer radiation belt: Multi dimensional phase space density analysis. *Accepted to Geophysical Research Letters*, *50*(23). https://doi.org/10.1029/2023gl106162

Staples, F. A., Rae, I. J., Forsyth, C., Smith, A. R. A., Murphy, K. R., Raymer, K. M., et al. (2020). Do statistical models capture the dynamics of the magnetopause during sudden magnetospheric compressions? *Journal of Geophysical Research: Space Physics*, *125*(4), e2019JA027289. https://doi.org/10.1029/2019JA027289

Subbotin, D. A., & Shprits, Y. Y. (2009). Three-dimensional modeling of the radiation belts using the Versatile Electron Radiation Belt (VERB) code. *Space Weather*, *7*(10). https://doi.org/10.1029/2008SW000452

Thébault, E., Finlay, C. C., Beggan, C. D., Alken, P., Aubert, J., Barrois, O., et al. (2015). International geomagnetic reference field: The 12th generation. *Earth Planets and Space*, *67*(1), 79. https://doi.org/10.1186/s40623-015-0228-9

Tsyganenko, N. A. (1989). A magnetospheric magnetic field model with a warped tail current sheet. *Planetary and Space Science*, *37*(1), 5–20. https://doi.org/10.1016/0032-0633(89)90066-4

Turner, D. L., & Li, X. (2011). Using spacecraft measurements ahead of Earth in the Parker spiral to improve terrestrial space weather forecasts. *Space Weather*, *9*(1). https://doi.org/10.1029/2010SW000627

Tuszewski, M., Cayton, T. E., Ingraham, J. C., & Kippen, R. M. (2004). Bremsstrahlung effects in energetic particle detectors. *Space Weather*, *2*(10). https://doi.org/10.1029/2003SW000057

Walt, M. (1994). *Introduction to geomagnetically trapped radiation*. Cambridge University Press.

Watt, C. E. J., Allison, H. J., Meredith, N. P., Thompson, R. L., Bentley, S. N., Rae, I. J., et al. (2019). Variability of quasilinear diffusion coefficients for plasmaspheric hiss. *Journal of Geophysical Research: Space Physics*, *124*(11), 8488–8506. https://doi.org/10.1029/2018JA026401

Wei, L., Zhong, Q., Lin, R., Wang, J., Liu, S., & Cao, Y. (2018). Quantitative prediction of high-energy electron integral flux at geostationary orbit based on deep learning. *Space Weather*, *16*(7), 903–916. https://doi.org/10.1029/2018SW001829

Wong, J.-M., Meredith, N. P., Horne, R. B., Glauert, S. A., & Ross, J. P. J. (2024). New chorus diffusion coefficients for radiation belt modeling. *Journal of Geophysical Research: Space Physics*, *129*(1), e2023JA031607. https://doi.org/10.1029/2023JA031607

Zhao, H., Friedel, R. H. W., Chen, Y., Reeves, G. D., Baker, D. N., Li, X., et al. (2018). An empirical model of radiation belt electron pitch angle distributions based on Van Allen probes measurements. *Journal of Geophysical Research: Space Physics*, *123*(5), 3493–3511. https://doi.org/10.1029/2018JA025277